PHYSICAL REVIEW B **77**, 094433 (2008)

Resonant magnetic x-ray scattering in the antiferromagnet $Ce(Fe_{1-x}Co_x)_2$

L. Paolasini,[1] S. Di Matteo,[2] P. P. Deen,[1,*] S. Wilkins,[1,†] C. Mazzoli,[1] B. Detlefs,[3,‡] G. Lapertot,[4] and P. Canfield[5]
[1]*European Synchrotron Radiation Facility, Bôite Postale 220, 38043 Grenoble, France*
[2]*Equipe de Physique des Surfaces et Interfaces, Institut de Physique de Rennes, UMR UR1-CNRS 6251, Université de Rennes 1, F-35042 Rennes Cedex, France*
[3]*European Commission, JRC, Institut for Transuranium Elements, Postfach 2340, D-76125 Karlsruhe, Germany*
[4]*Département de Recherche Fondamentale sur la Matière Condenée, SPSMS, CEA, 38054 Grenoble Cedex 9, France*
[5]*Ames Laboratory, Iowa State University, Ames, Iowa 50011, USA*

(Received 26 February 2007; revised manuscript received 18 December 2007; published 27 March 2008)

Magnetic resonant x-ray scattering experiments have been performed in Co-doped $CeFe_2$ at Ce $L_{2,3}$ and Fe K edges in the antiferromagnetic state. We could confirm a previous result that Ce moments lie parallel to the distortion rhombohedral axis $\langle 111 \rangle$ and Fe magnetic moments are arranged in a noncollinear structure by combining experimental data and numerical *ab initio* calculations at the Fe K edge. Interestingly, we were also able to qualitatively reproduce the main three peaks in the energy scan at Ce L edges by means of single-particle relativistic multiple-scattering calculations, provided that we extend the cluster radius up to the third shell of Ce nearest neighbors. We not only proved the main dipolar character of these resonances but also identified a non-negligible quadrupolar contribution. These results have suggested analyzing the orbital character of each peak through an azimuth scan. Experimentally, only the lower-energy peak showed the azimuth modulation expected for a quadrupolar transition. These findings, pointing to a single energy-position of $4f$ states, have a natural theoretical framework in a "monovalence" model, instead of the usually adopted "mixed-valence" model. Further analysis in the future would be desirable to clarify this fundamental issue. Finally, the magnetic phase diagram under applied magnetic field is also reported and compared to previous neutron scattering data.

DOI: 10.1103/PhysRevB.77.094433 PACS number(s): 75.50.Ee, 75.25.+z, 71.20.Eh, 71.30.+h

I. INTRODUCTION

$CeFe_2$ is a C15 Laves phase system of particular interest: If compared to the isostructural rare-earth iron materials of composition $REFe_2$, it is characterized by anomalous ferromagnetism, with unusually low Curie temperature ($T_C = 235$ K), small magnetization, and anomalous low temperature resistivity behavior. It has therefore stimulated many experimental and theoretical investigations in the past two decades. One of the main debates was focused on the interplay between Fe $3d$ and Ce $4f$ orbitals and whether the delocalization of Ce $4f$ orbitals due to band formation could play a major role in the determination of magnetic properties.

On the theoretical side, the first descriptions were given in terms of localized $4f$ states and had pointed toward the so-called mixed-valence (or fluctuating-valence) behavior of Ce ions,[1] whose ground state was then described as a superposition of $|4f^0\rangle$ and $|4f^1\rangle$ configurations. Such a superposition was required to explain the presence of a second peak at Ce $L_{2,3}$-edges absorption spectra, which are about 6 eV higher in energy than the white line. In this framework, photoemission spectra could be properly described through a single impurity Anderson model (SIAM) by invoking final-state effects from the mixed-valence state.[2,3] With this treatment, the three peaks in the photoemission spectrum were identified as the signature of $4f^2$, $4f^1$, and $4f^0$ states, a typical many-body effect. However, in 1988, Eriksson *et al.*[4] provided us with a theoretical description of this material in terms of the itinerant character of Ce $4f$ electrons, through a single-particle picture, and explained the anomaly of lattice constants in terms of $3d$-$4f$ hybridization rather than a valence change within Ce^{3+}-ion. The ambiguity, and even contradictory character, of the two theoretical descriptions of the spectroscopic data is apparent in the study of Konishi *et al.*,[5] who performed calculations with both the many-body approach of SIAM and the single-particle approach of density functional theory (DFT), and could describe the main features of the spectroscopic data with both approaches. They concluded by posing the question of how the so-called Kondo peak (the $4f^1$ final state) of the SIAM picture and the $4f$ band of the band picture are related to each other since, according the DFT, this peak is a one-electron feature and, in the SIAM, this is due to a many-body effect.

On the experimental side, the photoemission and Ce L-edges x-ray absorption data were invigorated by x-ray magnetic circular dichroism (XMCD) measurements, which were again interpreted in terms of the mixed-valence ground state because of a peculiar double-peak shape in the energy dependence of XMCD, which was absent in the isostructural $REFe_2$ (RE=Gd, Hf, and Lu).[6] A fitting procedure[3] was then used to extract the degree of ionization of Ce ions based on the fact that, in the theoretical modelization adopted in Refs. 3 and 6, the peaks belonged to two differently screened ionic configurations.

More recently, the production of large single crystals of $CeFe_2$ opened the avenue to magnetic inelastic neutron scattering experiments, which showed strong *antiferromagnetic* (AF) fluctuations at the $(\frac{1}{2}\frac{1}{2}\frac{1}{2})$ reciprocal lattice point, despite the nominal ferrimagnetic character of this material, as seen by magnetization and specific heat measurements.[7] These AF fluctuations are stabilized by a small amount of Co doping in substitution of Fe. However, the magnetic structure of the AF ground state had remained controversial up to very recently, where a combined set of experiments using neutron and resonant x-ray magnetic scattering (RXMS) have shed more light on the unusual magnetic ground state of pure and Co-doped $CeFe_2$.[8] The resulting model shows an AF ground state with a noncollinear magnetic structure on the Fe sublattice which breaks the frustrated AF configuration of the cubic lattice, inducing a rhombohedral lattice distortion, as found in $REFe_2$ (RE=Tb, Er, Ho, and Tm) compounds which develop giant spontaneous magnetostriction.[9] The proposed long-range noncollinear structure in the low temperature AF phase rationalizes many of the unusual and conflicting experimental results, as reported in the literature for this material,[10–12] and can explain the dynamical properties of the magnetic ground state in pure $CeFe_2$, as observed in inelastic neutron scattering experiments.[13]

The present paper draws on the magnetic-structure determination of Ref. 8, to confirm its main results through an *ab initio* analysis at Fe K edge and aims at clarifying several other open points. In the first place, we describe in detail the RXMS studies of the AF ground state of Co-doped $CeFe_2$ single crystals at Ce L edges. We highlight the importance of RXMS to get information on the magnetic density of states as a complementary tool of XMCD. The data are interpreted both in terms of a phenomenological formula and in terms of *ab initio* numerical calculations based on the FDMNES program.[14] The first approach allows recognizing the importance of nonresonant magnetic contributions of Fe ions at Ce L edges. At the same time, it permits a direct comparison with the fitting procedure of XMCD data,[6] with the advantage of a bigger energy sensitivity and the possibility of measuring several reflections, which allow disentangling the lower-energy shoulder of the first resonant magnetic peak. The *ab initio* approach gives then access to the magnetic density of states projected on the resonant Ce ion. Interestingly enough, we could get a proper qualitative description of several features of RXMS at Ce $L_{2,3}$ edges by means of the monoelectronic, muffin-tin relativistic multiple-scattering subprogram of the FDMNES code.[14,15] In particular, the typical double-peak structure of the absorption and magnetic dichroism spectra,[6] which was usually interpreted as a consequence of final-state effects in the framework of the mixed-valence character of Ce ground state,[1,3,6] is qualitatively reproduced by our calculations. We then discuss the possible implications of these contradictory descriptions (i.e., mixed-valence vs monovalence) at least where spectroscopy interpretations at Ce L edges are concerned and perform an experimental verification to test which of the two physical mechanisms is at work. Finally, we describe the RXMS measurements performed at Ce L edge in an applied magnetic field and compare the temperature dependence of the Ce sublattice magnetic reflections with the available neutron-scattering and magnetization data.

II. EXPERIMENTAL DETAILS

RXMS experiments were performed at the ID20 beamline (ESRF, Grenoble) at the Ce $L_{2,3}$ edges and at the Fe K edge by tuning two undulators with period of 35 mm to the first harmonic to provide photons with a high degree of horizontal linear polarization. A nitrogen-cooled Si(111) double crystal monochromator, which is inserted between two vertical focusing Si mirrors, defined a narrow energy window whose full width at half maximum (FWHM) is 0.8 eV at 8 keV. The beam size at the sample position was $0.5\times 0.5\ \mathrm{mm}^2$ and the photon flux was about 10^{13} photons/s. RXMS experiments were performed by using a standard four circles diffractometer in the vertical scattering geometry (incident photon polarization σ) and an azimuthal arm with a standard closed cycle refrigerator. High magnetic field experiments were performed on a six circle diffractometer in the horizontal scattering geometry (incident photon polarization π), which supports a split-coil superconducting magnet with a vertical magnetic field of 10 T built by Oxford Instruments Superconductivity. The custom internal design of the magnet allows us to perform RXMS at low energies and with wide scattering angles.[16]

A polarization analyzer is assembled on the detector arms of both diffractometers, and a LiF(220) analyzer was used to discriminate the linear polarization of scattered photons at L_3 ($E=5.720$ keV) and L_2 ($E=6.160$ keV) edges of Ce. The mosaic spreads of the LiF(220) analyzer were 0.052(2)° and 0.034(3)° in the $\sigma-\sigma'$ and $\sigma-\pi'$ channels, respectively, and the cross-talks determined on a charge peak (222) were 4% and 1% at L_3 and L_2 edges of Ce, respectively. Polarization analysis at the K edge of Fe was also performed by mounting a MgO(111) crystal with a mosaic spread of 0.025(5)° in the $\sigma-\pi'$ channel and a cross-talk better than 0.1%.

We selected small single crystals of $Ce(Fe_{1-x}Co_x)_2$, with $x=0.07$ and 0.10 grown by a self-flux-growth method at the Ames Laboratory (Iowa State University).[17] $CeFe_2$ crystallizes in the cubic Laves phase structure (C15, space group $Fd\bar{3}m$) and the lattice parameters are reduced at room temperature from $a_0=7.308$ Å for the pure compound to $a_0=7.296$ Å and $a_0=7.293$ Å in the 7% and 10% doped materials, respectively, which are in good agreement with previous neutron powder diffraction.[18] The sample quality and composition were tested with magnetization, resistivity, specific heat, and electron spectroscopy. The effect of Co doping is to lower the ferromagnetic transition T_C from 220 K for the pure $CeFe_2$ to 200 K ($x=0.07$) and 190 K ($x=0.10$), whereas the AF transition (observable only in Co-doped samples) rises from $T_N=69$ K to $T_N=82$ K for the Co concentrations of $x=0.07$ and $x=0.10$, respectively.[19,20] The samples were cut in thin slices of $2\times 2\times 0.5\ \mathrm{mm}^3$ with the threefold axis [111] perpendicular to the scattering surface, which is glued with a silver paste on a copper sample holder.

A. Absorption corrections

The absorption coefficients are calculated from the fluorescence yield data, which are measured at Ce L_3 and L_2 absorption edges, with the incident photon beam nearly perpendicular to the surface [111] of the sample (takeoff angle of 10°), the detector at $2\theta=90°$, and the incident linear polarization was parallel to the $[11\bar{2}]$ axis (Fig. 1). The spectra were fitted using the following function convoluted with a

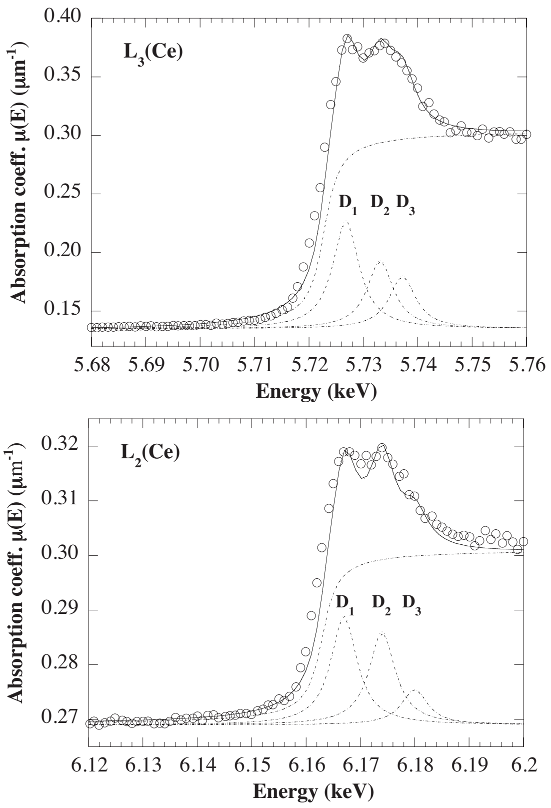

FIG. 1. XANES spectra at L_3 (upper panel) and L_2 (lower panel) edges of Ce taken at $T=13$ K. The data are collected in fluorescence mode and are normalized in terms of absorption coefficient. The solid lines correspond to the fit described in the text according to Eq. (1).

Gaussian resolution function whose FWHM was 0.8 eV:

$$F(E) = \sum_{k=1,3} \frac{p_k}{(E-D_k)^2 + \Gamma^2/4} + \left[0.5 + \frac{1}{\pi}\arctan\left(\frac{E-\varepsilon}{\Gamma/2}\right)\right], \tag{1}$$

where E is the photon energy, D_k are the energy position of the excited $5d$ states, ε is the excitation energy into the continuum states, and p_k measure the strengths of the resonances. The Lorentzians describe the transitions to "quasiparticle" states of d symmetry when projected on the resonating Ce ion, and the arctan function describes the threshold to the continuum. Γ represents the core-hole lifetime.

Three Lorentzian functions are necessary to fit the peak structure in the x-ray appearance near-edge structure (XANES) region, which is in agreement with previous experimental absorption spectra.[21] The parameters obtained are summarized in Table I.

The absorption coefficient $\mu(E)$ can be calculated as a function of energy from the fluorescence data through[22]

$$\mu(E) = \mu_L + \frac{\mu_H - \mu_L}{F_H - F_L}[F(E) - F_L], \tag{2}$$

where F_H and F_L are the measured fluorescence yield $F(E)$ and μ_H and μ_L are the tabulated absorption coefficients above and below the absorption edges, respectively.[23]

The absorption coefficients $\mu(E)$ extracted by the fluorescence data were used for the absorption correction of the RMXS intensities. By taking into account the thick sample approximation, the resonant intensities can be calculated by

$$I_{corr} = I_{obs}\mu(E)\left(1 + \frac{\sin\alpha_0}{\sin\alpha_1}\right), \tag{3}$$

where α_0 and α_1 are the incident and reflected angles of the beam with the sample. This expression is simplified in the case of specular reflections ($\alpha_0=\alpha_1$).

III. EXPERIMENTAL RESULTS

At low temperature, Ce(Co$_{0.07}$Fe$_{0.93}$)$_2$ becomes AF with an ordering wave vector $q_M=(\frac{1}{2},\frac{1}{2},\frac{1}{2})$. This transition is accompanied by a rhombohedral crystallographic distortion ($\alpha=90.31°$) with a decrease of about 0.2% in volume.[13] The rhombohedral distortion results in the body diagonal becoming shorter in the AF ground state.

When the diffractometer is set to the (222) position, for $T<T_N$, the four peaks observed as a function of the rocking angle correspond to these individual crystallographic domains (large detector slits are used in these specific scans). The high Q resolution due to the small divergence of the photon beam allows the separation of the individual rhombohedral domains, as shown in Fig. 2. For each crystallographic domain, we found the corresponding magnetic satellites with a propagation vector q_M which were well separated in the reciprocal space. The FWHM of the Bragg peak (222)

TABLE I. Data obtained by the fit of the fluorescence yield at Ce L_3 and L_2 edges using Eq. (1). The data are expressed in eV and the standard deviations refer to the least-significant digit.

Edge	Energy	ε	Γ	D_k	Γ
L_3	5723	5721.8(2)	3.7(3)	D_1 5726.9(2)	6.4(4)
				D_2 5733.5(5)	6.4(4)
				D_3 5737.8(3)	6.4(4)
L_2	6163	6161.0(3)	3.7(4)	D_1 6167.3(4)	6.4(5)
				D_2 6174.3(6)	6.4(5)
				D_3 6178.4(3)	6.4(5)

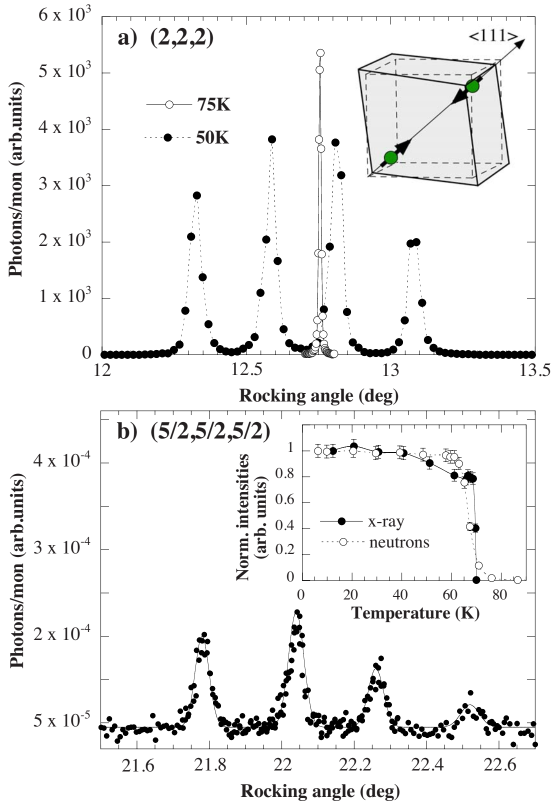

FIG. 2. (Color online) (a) Crystallographic and (b) magnetic domain formations in the 7% Co doped $CeFe_2$: (a) (222) Bragg reflection measured at 75 K (open circles) above the rhombohedral distortion and at 50 K (closed circles) in the antiferromagnetic phase. The inset shows the rhombohedral distortion of the cubic unit cell and the relative directions of the Ce magnetic moments (thick arrows). (b) $(\frac{5}{2},\frac{5}{2},\frac{5}{2})$ magnetic domains measured at the nonresonant energy E=5.600 keV in the $\sigma-\pi'$ channel. The inset shows the temperature dependence of the integrated intensities of the AF reflection $(\frac{5}{2},\frac{5}{2},\frac{5}{2})$ measured by neutron scattering (open circles) and x-ray scattering (closed circles).

above T_N=69 K was about 0.010(3)° and after the distortion, it increased to about 0.050(5)°. These data are taken at E =5.600 keV in nonresonant conditions, which is about 200 eV below the L_3 absorption edge of Ce. The magnetic reflections abruptly disappeared above T_N=69 K, as shown in the inset of Fig. 2. Thermal cycling around T_N strongly influences the magnetic domain population, giving rise to different saturated magnetic intensities.

When the photon energy is tuned across the L_3 and L_2 Ce absorption edges, the magnetic signal at the AF reflections is greatly enhanced, as shown in Figs. 3 and 4 for some specular AF reflections. The scans are collected in the rotated $\sigma-\pi'$ polarization channel in the 7% Co-doped sample, and they are corrected for the absorption coefficient $\mu(E)$, as described previously. The $\sigma-\sigma'$ polarization channel does not show any resonant enhancement, as expected for Ce magnetic moments directed along the [111] direction and parallel to the scattering vector. The spectral shape is similar at the L_2 and L_3 edges, with three major peaks at energies E_1, E_2, and E_3, as indicated by the arrows in Figs. 3 and 4, which are reported in Table II. It is interesting to note that it was not possible to resolve the first two, lower-lying peaks by means of XMCD experiments in the pure compound.[6] The L_3 and L_2 spectra can be fitted very well through the sum of three Lorentzians with a background given by the nonresonant magnetic scattering due to Fe atoms: The fitting procedure is then compared to the results existing in the literature for L-edges absorption, photoemission, and XMCD.[5,6]

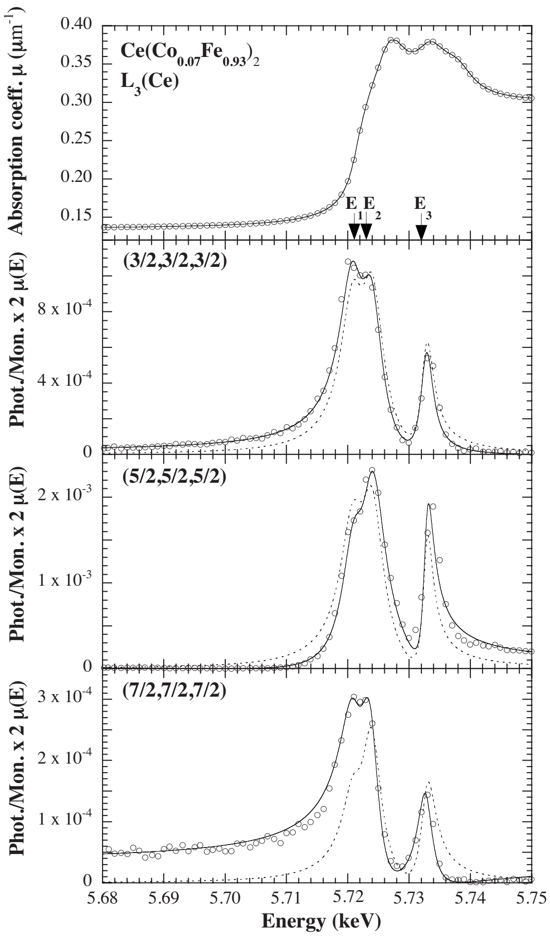

FIG. 3. Energy dependence of RXMS intensities collected at T=12 K in $\sigma-\pi'$ polarization channel across the L_3 edge of Ce for specular magnetic reflections. The magnetic intensities are corrected for the absorption coefficient 2μ (top panel) following the fitting procedure described in the text (continuous lines). The broken lines are the results of the fit without the nonresonant contribution.

In order to extract the pure resonant contribution from the experimental data, we use the following expression for the absorption corrected intensities:

$$I_{corr} = I_0\left[\left(1+\sum_{i=1}^{3}A_i^{res}\frac{x_i}{x_i^2+1}\right)^2+\left(\sum_{i=1}^{3}A_i^{res}\frac{1}{x_i^2+1}\right)^2\right], \tag{4}$$

where A_i^{res} are the resonant amplitudes [e.g., the numerator of Eq. (5)] normalized with respect to the nonresonant magnetic scattering amplitude. The Lorentzian energy line shape for each resonance is contained in the reduced energy term x_i

$=\frac{\hbar\omega-E_i}{\Gamma_i/2}$, where Γ_i is the core-hole lifetime convoluted with the instrument resolution. In order to get a faster convergence of the fit, we used the constraint $\Gamma_1=\Gamma_2$. The broken lines in Figs. 3 and 4 are obtained by using the fitted parameter reported in Table II without the nonresonant contribution and will be directly used to compare with the theoretical *ab initio* calculations, as described in the next section. As clear from Figs. 3 and 4, the Fano-like line shape determined by the coherent interference between different resonant and nonresonant processes is enhanced over a broad energy range far from the absorption edges because of the broad Γ linewidth of each single resonance. The ratio between the resonant amplitudes A_i^{res} at the L edges within the same Bragg reflections can also be directly related to the experimental data taken by XMCD in the ferromagnetic state.[6] Some comments are now necessary in order to compare these results with those from XMCD. In first place, our RXMS experiments allow a better determination of the lower-energy feature, at energy E_1, which could not be resolved from the one at energy E_2 in the XMCD experiment.[6] Moreover, as described in the next section, quadrupolar transitions play a role in the RXMS case, through interference effects which were not detectable with XMCD. We found that the energy splitting between E_3 and $(E_1+E_2)/2$, $\sim$10 eV, is very close to the splitting of the two features measured with XMCD. Therefore, we can safely conclude that the two techniques have basically access to the same magnetic density of states, although RXMS has the advantage that there are interference effects that allow a better identification of the individual contributions. Notice that the three peaks of RXMS may be the analogous of the three features in the photoemission experiments, which are usually interpreted (in a SIAM framework) as a signature of $4f^0$, $4f^1$, and $4f^2$ final states (even though some care should be taken, as the core-hole potential is different in the two cases).[5]

It is interesting to underline also that the nonresonant magnetic contribution determined mainly by Fe-ions interferes with the resonant scattering amplitudes [see Eq. (4)] and its effect is fundamental to explain the behavior of the signal far from Ce L-absorption edges. In fact, due to the opposite relative sign in the amplitude at L_3 and L_2 edges, for the same AF reflection the two signals add or subtract, respectively, and this determines the opposite behavior of the tails at higher and/or lower energies at the two edges. Moreover, the interference effects is a function of the scattering vector due to the change in sign of L_3 and L_2 amplitudes when wave vectors differ by (111) [see Eq. (6) below]: This is the origin of the opposite behavior of the $(\frac{5}{2},\frac{5}{2},\frac{5}{2})$ compared to $(\frac{3}{2},\frac{3}{2},\frac{3}{2})$ and $(\frac{7}{2},\frac{7}{2},\frac{7}{2})$.

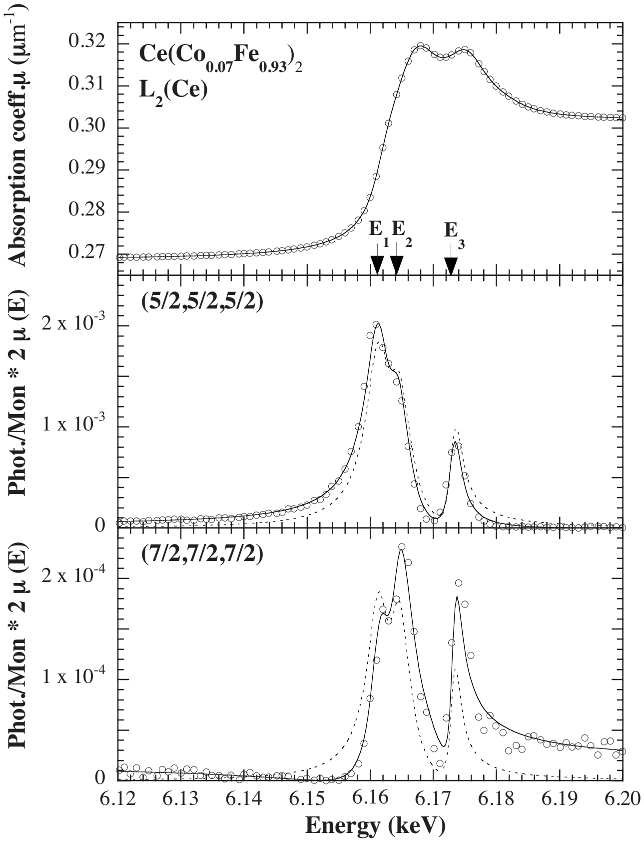

FIG. 4. Energy dependence of resonant magnetic scattering intensities collected at $T=12$ K in $\sigma-\pi'$ channel at the L_2 edge for two specular magnetic Bragg reflections. The data are corrected for absorption, as in Fig. 3.

TABLE II. Data obtained by the fit (as described in the text) of RXMS spectra at Ce L_3 and L_2 absorption edges for different specular AF reflections $(\frac{l}{2},\frac{l}{2},\frac{l}{2})$. The standard deviations refer to the least-significant digit.

	E_1 (eV)	E_2 (eV)	E_3 (eV)	$\Delta(E_2-E_1)$ (eV)	$\Delta(E_3-E_1)$ (eV)
L_3	5721.0(2)	5723.9(3)	5732.8(3)	2.8(2)	11.8(2)
L_2	6161.5(3)	6164.5(4)	6173.5(2)	3.0(1)	9.0(3)

(h,k,l)	L_i	$I_0\times10^5$	A_1	A_2	A_3	Γ_1,Γ_2	Γ_3
$(\frac{3}{2},\frac{3}{2},\frac{3}{2})$	L_3	1.2(6)	−5.6(2)	−6.7(3)	−2.7(2)	4.5(3)	3.0(4)
$(\frac{5}{2},\frac{5}{2},\frac{5}{2})$	L_3	5.0(8)	+3.7(2)	+4.9(2)	+4.6(1)	4.6(4)	2.0(3)
	L_2	2.0(5)	−6.8(3)	−5.9(3)	−5.6(2)	4.5(3)	2.5(3)
$(\frac{7}{2},\frac{7}{2},\frac{7}{2})$	L_3	3.2(5)	−1.1(2)	−2.4(3)	−1.9(2)	4.0(4)	3.0(3)
	L_2	1.7(5)	+2.3(2)	+2.4(2)	+2.1(3)	4.0(2)	2.0(4)

IV. *AB INITIO* CALCULATIONS AND DISCUSSION

In resonant x-ray scattering, the global process of photon absorption, i.e., virtual photoelectron excitation and photon re-emission, is coherent throughout the crystal, thus giving rise to the usual Bragg diffraction condition: $\Sigma_j e^{i\vec{Q}\cdot\vec{R}_j}(f_{0j}+f'_j+if''_j)$. Here, $\vec{R}_j$ stands for the position of the scattering ion j, $\vec{Q}$ is the diffraction vector, and f_{0j} is the Thomson amplitude or the nonresonant magnetic scattering amplitude of the jth atom. The resonant part $f'_j+if''_j$, i.e., the anomalous atomic scattering factor (ASF), is given by[24]

$$f'_j + if''_j \equiv f_j(\omega) \propto -\omega^2 \sum_n \frac{\langle \psi_g(j)|\hat{O}^*_o|\psi_n\rangle\langle\psi_n|\hat{O}_i|\psi_g(j)\rangle}{\hbar\omega - (E_n - E_g) - i\frac{\Gamma_n}{2}}, \tag{5}$$

where $\hbar\omega$ is the photon energy, E_g the ground state energy, and E_n and Γ_n are the energy and inverse lifetime of the excited states. $\psi_g(j)$ is the core ground state centered around the jth atom and ψ_n is the photoexcited state. The sum is extended over all the excited states of the system. The transition operator $\hat{O}_{i(o)}=\vec{\epsilon}_{i(o)}\cdot\vec{r}(1-\frac{i}{2}\vec{q}_{i(o)}\cdot\vec{r})$ is written through the multipolar expansion of the photon field up to electric dipole (E1) and quadrupole (E2) terms; $\vec{r}$ is the electron position measured from the resonant ion, $\vec{\epsilon}_{i(o)}$ is the polarization of the incoming (outgoing) photon, and $\vec{q}_{i(o)}$ is its corresponding wave vector. The previous set of equations form the basis for our numerical calculation through the FDMNES program.[15] The main difficulty in the evaluation of the ASF is the determination of the excited states by means of some *ab initio* procedure. In the following, we shall use a relativistic extension of the muffin-tin, multiple-scattering approach in the FDMNES code[15] that, although monoelectronic, includes the spin-orbit interaction and allows us to handle magnetic processes.

A. Fe *K* edge

As a first thing, we want to comment on the theoretical interpretation of previous measurements performed at the Fe *K* edge in order to double check the consistency of some results of Ref. 8 that had not been yet verified by calculations. Experimental results of the magnetic reflection $(\frac{5}{2},\frac{5}{2},\frac{5}{2})$ at Fe *K* edge are shown in Fig. 5. A simple feature at the pre-edge appears, which was classified as dipolar in origin in Ref. 8 on the basis of its azimuthal scan and in agreement with the noncollinear magnetic structure of the Fe sublattice determined by elastic neutron diffraction (as shown in Fig. 6). It should be noted, however, that also E2-E2 signals can have a $\sin^2\phi$ azimuthal scan and therefore this assignment cannot be performed with certainty without an actual *ab initio* calculation.

The simulation has been performed in the multiple-scattering muffin-tin magnetic mode in two steps in order to take into account the noncollinearity of iron magnetic moments: A first calculation with Fe $1b$ site with a magnetic moment along the $[1\bar{1}0]$ direction and the Fe $3e$ sites with spherical symmetry has been superimposed to a calculation where the $3e$ sites were endowed with magnetic moment along the $[111]$ direction and the $1b$ site was taken as spherically symmetric. Such a approach relies on the independence of the two effects, which can be therefore linearly superimposed in their amplitudes to build the total intensity. In doing this, we neglect any possible correlation effect of one configuration over the other. However, *a posteriori*, a simple comparison of the calculated energy scan in Fig. 5 with the experimental one highlights the relatively good approximation performed. The azimuthal scan (not shown) is characterized by a sinusoidal modulation of a constant term, as experimentally found. The constant azimuthal scan is expected due to the $3e$-sites with magnetic moments along the $[111]$ direction (the signal is proportional to the projection of the magnetic moment along the outgoing wave vector k') and the sinusoidal modulation is determined by the $1b$ site, which

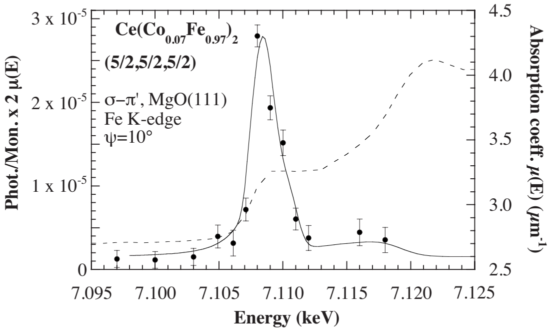

FIG. 5. Energy dependence of RXMS intensities (dots) collected across the Fe *K* edge in the rotated $\sigma-\pi'$ polarization channel (from Ref. 8). The continuous line is the *ab initio* calculation with the FDMNES program (Ref. 14) and the broken line represents the photoabsorption coefficient collected in the fluorescence yield mode.

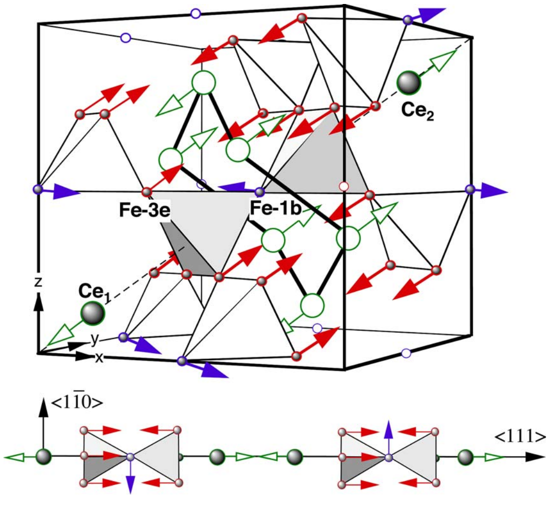

FIG. 6. (Color online) Primitive cubic cell ($Fd\bar{3}m$) and low temperature magnetic structure of $Ce(Co_{0.07}Fe_{0.93})_2$ determined by combined neutron and x-ray scattering experiments. The open arrows indicate the $\langle 111\rangle$ direction of the Ce magnetic moments, whereas the closed arrows show the two noncollinear Fe magnetic moment directions along the $\langle 111\rangle$ direction for the Fe $3e$ site and along $\langle 1\bar{1}0\rangle$ for the Fe $1b$ site (from Ref. 8).

sum up out of phase due to an imaginary unit in the Bragg term.

The actual calculation has shown that the signal, although at an energy usually assigned to quadrupolar transitions, is of purely E1-E1 origin, i.e., it is determined by the projection on the resonating ion of states with a global p symmetry. There is a very small admixture of quadrupolar terms (less than 2%) that gives a modulation of the azimuthal scan which is, however, below the present experimental sensitivity. This therefore confirms the conclusions of Ref. 8 regarding the noncollinear magnetic structure of the Fe sublattice, which is in accord with neutron magnetic diffraction results.

B. Ce L edge

Before analyzing the signal at Ce $L_{2,3}$ edges numerically, we find it useful to push analytical considerations as far as possible. Ce ions occupy $2c$ positions in the crystallographic $R\bar{3}m$ unit cell, with local symmetry $\bar{3}m$, lacking of inversion center. The structural coordinates are $\mathrm{Ce}_1=(x,x,x)$ and $\mathrm{Ce}_2=(\bar{x},\bar{x},\bar{x})$ in the trigonal set, with $x\simeq\frac{1}{8}$.[25] In the antiferromagnetic phase, the unit cell is doubled along the $\langle 111\rangle$ directions (see Fig. 6), which makes reflection of the kind $\{\frac{l}{2},\frac{l}{2},\frac{l}{2}\}$ magnetically allowed.[8] For this class of reflection, the structure factor is

$$f\left(\frac{l}{2},\frac{l}{2},\frac{l}{2}\right)=e^{3\pi i(l/8)}f_{\mathrm{Ce}_1}+e^{-3\pi i(l/8)}f_{\mathrm{Ce}_2}, \tag{6}$$

and the two ASF are related by inversion symmetry, i.e., $f_{\mathrm{Ce}_2}=\hat{I}f_{\mathrm{Ce}_1}$. This means $f_{\mathrm{Ce}_2}=f_{\mathrm{Ce}_1}$ for E1-E1 and E2-E2 transitions, which are parity-even, and $f_{\mathrm{Ce}_2}=-f_{\mathrm{Ce}_1}$ for E1-E2 transitions, which are parity-odd. At the three reflections under study, $l=3,5,7$ and specifically

$$f\left(\frac{3}{2},\frac{3}{2},\frac{3}{2}\right)=-2i\sin(\pi/8)f^{(+)}_{\mathrm{Ce}_1}-2\cos(\pi/8)f^{(-)}_{\mathrm{Ce}_1},$$

$$f\left(\frac{5}{2},\frac{5}{2},\frac{5}{2}\right)=-2i\sin(\pi/8)f^{(+)}_{\mathrm{Ce}_1}+2\cos(\pi/8)f^{(-)}_{\mathrm{Ce}_1},$$

$$f\left(\frac{7}{2},\frac{7}{2},\frac{7}{2}\right)=2i\sin(3\pi/8)f^{(+)}_{\mathrm{Ce}_1}-2\cos(3\pi/8)f^{(-)}_{\mathrm{Ce}_1}, \tag{7}$$

where $f^{(+)}_{\mathrm{Ce}_1}$ is the ASF of E1-E1 and E2-E2 origins (parity-even) and $f^{(-)}_{\mathrm{Ce}_1}$ is the ASF of E1-E2 origin (parity-odd). All the previous quantities are purely magnetic. It is important to stress that E1-E2 terms bring an extra imaginary unit so that the $f^{(+)}_{\mathrm{Ce}_1}$ and the $f^{(-)}_{\mathrm{Ce}_1}$ do actually interfere. It is interesting to note also that the factor $\cos(\pi/8)\simeq 0.92$ enhances the E1-E2 terms with respect to the E1-E1 at $(\frac{3}{2},\frac{3}{2},\frac{3}{2})$ and $(\frac{5}{2},\frac{5}{2},\frac{5}{2})$, where $\sin(\pi/8)\simeq 0.38$. The opposite is true for the $(\frac{7}{2},\frac{7}{2},\frac{7}{2})$ reflection.

In Fig. 7, we show the results of our numerical calculations at the L_3 edge for all the reflections reported in Fig. 3. The agreement with the experiment, although only qualitative under some aspects, shows a remarkable feature: the presence of the triple-peak structure, which is usually explained through a mixed-valence model. In this latter model, the three-peak structure is attributed to the dynamical ground state of Ce^{3+} ion, which is a linear superposition of a $4f^05d^1$ and a $4f^15d^0$ configurations.[1,5,6] It therefore reflects the possible screening mechanisms of the $2p$ core hole, either well screened by a $4f$ electron or poorly screened by a $5d$ electron, i.e., it represents a final-state effect (either $4f^05d^2$, or $4f^15d^1$, or $4f^25d^0$).

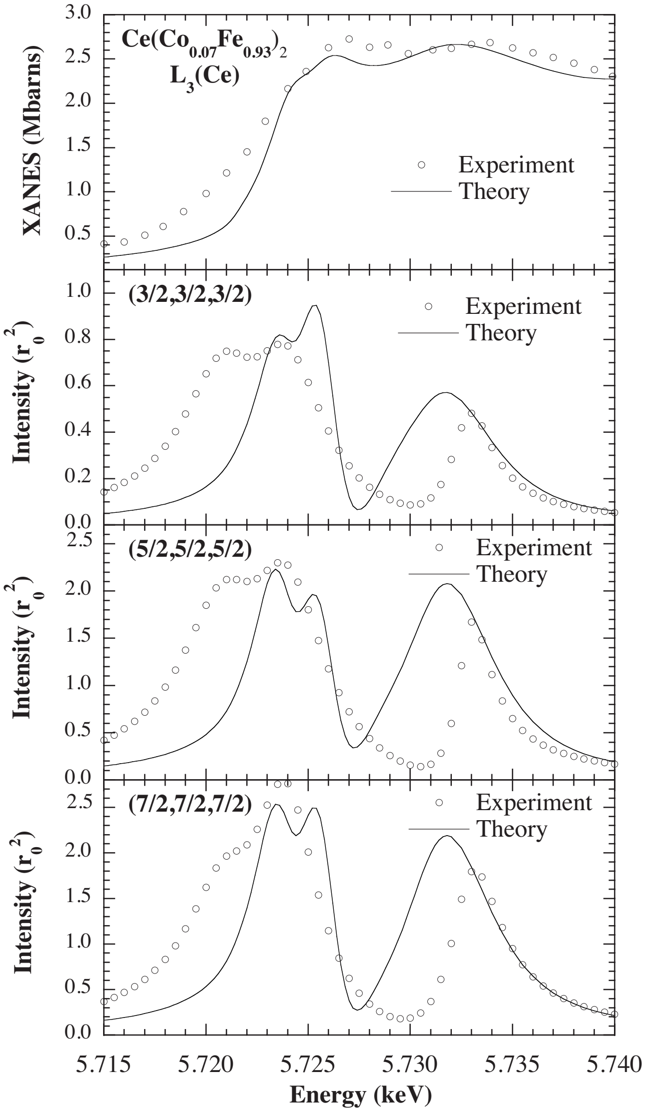

FIG. 7. Experimental data (open circles) and calculated (lines) absorption and RXMS spectra of the AF reflections at the Ce L_3 edge. The experimental RMXS intensities are obtained by subtraction of the nonresonant magnetic x-ray signal using the fitting procedure, as described in Sec. II [Eq. (4)].

By construction, such an effect is absent in our *ab initio*, single-particle calculations and we should look for the origin of the three-peak structure elsewhere. As shown in Fig. 8, where we report the evolution of the spectral features with the radius of the multiple-scattering cluster, the origin is determined by multiple-scattering interference effects. In fact, if only one Ce-atom is taken into account, no splitting of the features is present in the magnetic density of states, but a

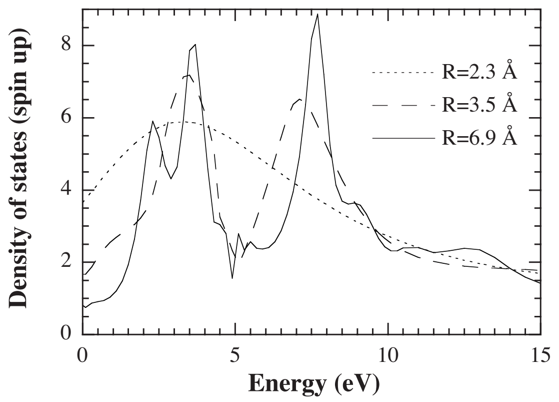

FIG. 8. Dependence of the $d_\uparrow$ density of states on the radius R of the cluster (expressed in angstrom units).

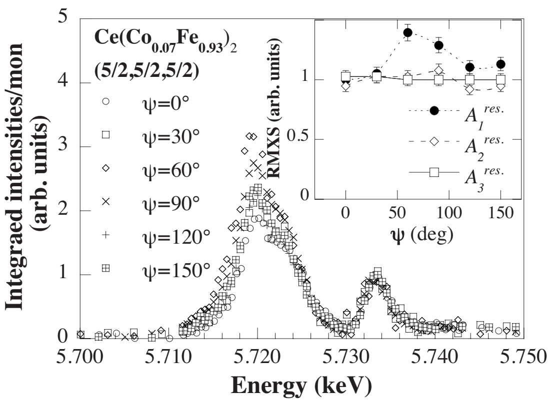

FIG. 9. Energy scans of the reflection $(\frac{5}{2},\frac{5}{2},\frac{5}{2})$ collected at different azimuth angles ψ and normalized at $E_3=5.733$ keV (rough data without absorption corrections). The inset shows the azimuthal dependence of the resonant amplitudes A_i^{res} determined by the fitting procedure described in Eq. (4), and normalized at E_3.

multipeak structure appears when the effect of nearest-neighbors Ce atoms is considered. It is interesting to note that the splitting of the lower-energy peaks (at energies E_1 and E_2) is determined by third-nearest neighbors (cluster radius of ~6.9 Å, i.e., 29 Ce atoms and 40 Fe atoms) and it appears as an effect of the cluster symmetry: In fact, the first and third Ce nearest neighbors share the same symmetry, i.e., a subgroup of the tetrahedral group, whereas Ce second nearest neighbors have a symmetry derived from the cubic one, which apparently does not play any role in this effect. This aspect may be related to the large extension of Ce wave functions that project with d symmetry over the resonating Ce ion.

We must say, however, that the agreement with the experiment is only qualitative because the energy gap between the higher-energy peak and the minimum between the two lower-energy peaks at, e.g., the $(\frac{3}{2},\frac{3}{2},\frac{3}{2})$ reflection is (experimentally) ~11 eV, whereas the calculated gap is ~7.5 eV. This problem might be specific of the single-particle potential used [as found already, for example, in V_2O_3 (Ref. 26)], and it is more probably the indication that many-body effects are needed to describe these spectra. The question is how it is possible that, in absorption and XMCD, only Ce-compounds are characterized by a double-peak structure, whereas other isostructural compounds, as $GdFe_2$ in Ref. 6, do not show such a structure. We might guess that the difference is determined by the total charge *and* the cell length, which give rise to different multiple-scattering paths and therefore different interference effects. A numerical calculation of XMCD for $CeFe_2$ has reproduced the double-peak structure (though energy compressed as for RXMS), whereas for $GdFe_2$, it has shown a single energy peak with a smaller shoulder at higher energy: This different behavior comes from the fact that in $GdFe_2$ the higher-energy peak is much closer to the lower-energy one (less than 3 eV) than in $CeFe_2$. However, a more systematic analysis is needed on this matter and will be the subject of a future work.

Another interesting aspect that comes out of our calculations is that a pure E1-E1 transition cannot explain the relative changes in intensity vs the wave vector of the two lower-energy peaks. In fact, in this case, the energy shape at all three reflections is the same for all wave vectors, weighted by the geometrical factors of Eq. (6). On the contrary, the interference with E1-E2 and E2-E2 terms can modify this shape, as these latter have different signs at different reflections ($l=3,5,7$). In our calculations, E1-E2 and E2-E2 amplitudes are of similar order of magnitude, which is about one-tenth of the E1-E1 amplitude and their contribution becomes appreciable just because of the interference with E1-E1 terms [see Eq. (7)]. Their position is a fingerprint of the energy level of $4f$ states (though, possibly, relaxed due to the core-hole potential).

The presence of non-negligible interference with quadrupolar contributions has suggested to us a way to test mixed-valence and monovalence models. The idea is related to the fact that in a general single-particle approach, there is just one energy where $4f$ states contribute, i.e., just one energy where quadrupolar contributions can play a role. On the contrary, in the mixed-valence model, one is expected to get quadrupolar contributions at all main peaks, which have $4f^2$, $4f^1$, and $4f^0$ origins, depending on the valence condition and final-state effects. Notice that the amplitude of the calculated variation can be up to 30% for the $(\frac{5}{2},\frac{5}{2},\frac{5}{2})$ reflection. These quadrupolar contributions can be identified due to the different azimuth dependence, which is threefold, whereas the E1-E1 terms have no azimuth dependence. The reason for the different behaviors is that E1-E1 contributions are coupled to a magnetic moment as $(\vec{\epsilon}_o^{\,*}\times\vec{\epsilon}_i)\cdot\vec{m}$, i.e., they measure the projection of the magnetic moment $\vec{m}$ on the outgoing wave vector and this projection is constant in the experimental geometry of the azimuthal scan. On the contrary, E1-E2 and E2-E2 magnetic contributions are both determined by a rank 3 spherical tensor,[30,31] whose azimuthal symmetry in the plane orthogonal to the [111] direction is threefold.

The data shown in Fig. 9, representing several energy scans of the $(\frac{5}{2},\frac{5}{2},\frac{5}{2})$ reflection taken at Ce L_3 edge for different azimuthal angles, seem consistent with the monovalence description. By using the fitting procedure described in Eq. (4), we can separate the different RXMS amplitudes A_i^{res} and determine their relative azimuthal dependence. The inset

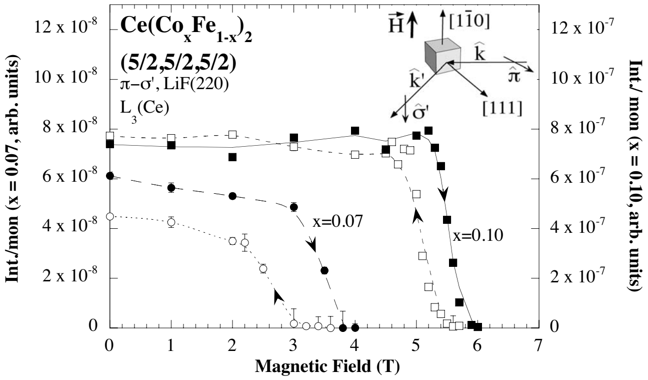

FIG. 10. Field dependence of the $(\frac{5}{2},\frac{5}{2},\frac{5}{2})$ magnetic reflection at Ce L_3 edge (E=5.721 keV) at 2.5 and 4 K for the 10% Co (circles) and 7% Co (square) doped samples, respectively. The arrows indicate the field hysteresis loop across the phase transition.

of Fig. 9 shows that the azimuthal dependence of A_1^{res} differs from the flat behavior of both A_2^{res} and A_3^{res} amplitudes, confirming the monovalence framework. However, more sensitive experiments and more precise theoretical calculations, which are beyond the scope of the present work, should be developed to frame our experimental results in a comprehensive theoretical model. On the theoretical side, a more precise estimation of the energy position of all $4f$ peaks is necessary, as well as a proper calculation of the relative amplitude compared to the corresponding $2p \rightarrow 5d$ E1 transitions, which requires correlation corrections that have not been taken into account in the present work. Moreover, precise SIAM calculations should be performed to check for an eventual compatibility of such a model with the experimental data of Fig. 9. On the experimental side, the measurement of a three-dimensional energy-azimuth plot with a precise determination of the relative intensities at all angles would require to go beyond the classical technique of rotating the sample, i.e., by adopting phase plates to rotate the incoming polarization.[27]

V. HIGH MAGNETIC FIELD MEASUREMENTS

For high magnetic field experiments, we have selected two crystals with 7% and 10% Co dopings, oriented with the cubic axis $[1\bar{1}0]$ parallel to the magnetic field. The data are collected at the Ce L_3 edge (E=5.721) in horizontal scattering plane, with π incident photon polarization, and analyzed in the rotated channel σ'. The RXMS intensities for the 10% sample are more than 1 order of magnitude stronger than those for the 7% doped sample, as we can see from Fig. 10. The magnetic field was applied at low temperature and subsequently increased up to the critical value, then decreased again. Typical hysteresis behavior is shown in Fig. 10 for both samples at low temperature. Large hysteresis is present for the sample with smaller doping of about 1 T at 4 K.

The difference in intensity between the field cooling (FC) and non-field-cooling reflects the different domain population due to the domain formation. Similar large hysteresis effects have been already observed in magnetization measurements, where the isothermal magnetization curves show an irreversible metamagnetic transition which is more pronounced at small Co concentrations.

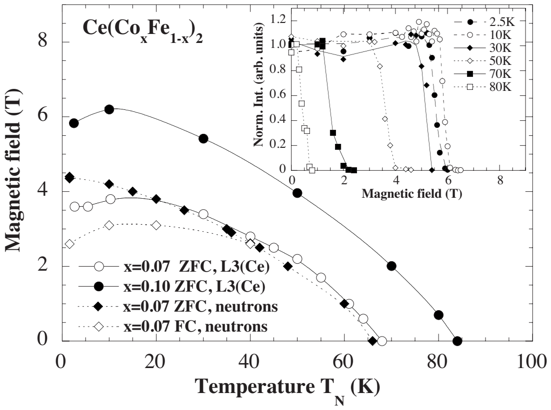

FIG. 11. Magnetic phase diagram determined for the 10% (closed circles) and 7% (open circles) Co doped samples. The neutron data for the 7% doped sample (diamonds) are taken from Ref. 13. The inset shows the zero field cooling RMXS intensities as a function of the magnetic field at different temperatures for the 10% Co doped sample.

The phase diagram obtained for the two samples is shown in Fig. 11, which is in accord with previous magnetization measurements.[28] Quite interestingly, at low temperatures the phase diagram shows a re-entrant behavior for both sample. In fact, as shown in the inset of Fig. 11 for the data collected in the 10% doped crystal, at 2.5 K, the critical field is 5.8 T, whereas at 10 K, it is 6.1 T. This effect was also observed in the neutron inelastic scattering experiments, as shown in Ref. 13, where a "quenched region" was observed in the FC inelastic spectra (open diamond in Fig. 11) with a coexistence of ferromagnetic and short-range AF fluctuations, whereas the zero field cooled neutron data reflect the phase diagram measured by magnetization.[28] Neutrons are more sensitive to the Fe magnetic moment, whereas the present RMXS is sensitive only to the Ce magnetic sublattice. Moreover, the bulk sensitivity of neutron scattering and the different time scales of the two techniques can be one of the reasons for the disagreement of the phase diagram at low temperature. Unfortunately, the weak resonant signal at Fe K edge does not allow a direct comparison of the field dependence of both the Ce and Fe sublattices, and future investigation is planned to this aim. The effect of the quenched disorder on the first order phase transition due to a magnetic phase coexistence was also highlighted in Ref. 29 on Ru-doped CeFe$_2$, where the temporal evolution was analyzed versus temperature and magnetization. Future work is planned to investigate the microscopic behavior of quenched disorder across the first order F-AF magnetic transition, which is responsible for the large magnetoresistance effects found in this compound at low temperature.

VI. SUMMARY AND CONCLUSIONS

We measured RXMS at Ce L-edges with and without magnetic field.

The measured AF spectra reproduce the magnetic density of states similarly to XMCD in the undoped compound. The better energy sensitivity allows us also to resolve the first two peaks, thanks to the interference effects that permitted us to single out E2 contributions due to their different azimuth dependence compared to E1.

We calculated the signal at the Fe *K* edge, with good agreement compared to previous experimental results[8] and confirmed in this way the correctness of the magnetic structure derived in Ref. 8.

We could qualitatively describe the experimental data at Ce *L* edges, for what the triple-peak structure is concerned, with a single-particle *ab initio* calculation. This poses the problem of the two contradictory descriptions, which are raised already in Ref. 5, compared to previous theoretical results found in the literature.[1,3,6] In order to clarify this issue, we have performed an experiment (see Fig. 9), which seems to point toward the structural origin of the three peaks structure in the magnetic density of states. Yet, more refined calculations to describe the azimuthal scan through the SIAM model than the deductions presented in this paper should probably be waited for before drawing definitive conclusions.

With this paper, we argue that the usual picture for explaning the double-peak structure in x-ray absorption and circular dicroism spectra of ferromagnetic $CeFe_2$ in terms of atomic mixed-valence ground state may be in need of correction. Whereas we do not reach a quantitative agreement with our single-particle *ab-initio* calculations, we believe that the many-body correlations needed to improve our description should be looked for in a "monovalence," extended-band framework, more than in atomistic "mixed-valence" models. This conclusion is derived from the experimental azimuth scan shown in Fig. 9, pointing to a single energy position of 4*f* states. However, more systematic information is required for a theoretical understanding of the interplay of atomic-multiplet configuration interactions and band-structure effects, which play important and often competing roles in strongly correlated electron systems.

ACKNOWLEDGMENTS

We wish to acknowledge François de Bergevin and Gerry Lander for stimulating discussions, J.-P. Valade for technical support at ID20, and Irina Snigireva for sample characterization by electron spectroscopy.

---

[*] Present address: Institut Laue-Langevin, Bôite Postale 156, 38042 Grenoble, France.

[†] Present address: Brookhaven National Laboratories, Upton, New York 11973-5000, USA.

[‡] Present address: European Synchrotron Radiation Facility, Bôite Postale 220, 38043 Grenoble, France.

[1] J. Röhler, *Handbook on Physics and Chemistry of Rare Earths*, edited by K. A. Gschneider and J. Hüfner (North-Holland, Amsterdam, 1987), Vol. 10, p. 453.

[2] K. Asakura, A. Kotani, and I. Harada, J. Phys. Soc. Jpn. **74**, 1328 (2005).

[3] D. Malterre, Phys. Rev. B **43**, 1391 (1991).

[4] O. Eriksson, L. Nordstrom, M. S. S. Brooks, and B. Johansson, Phys. Rev. Lett. **60**, 2523 (1988).

[5] T. Konishi, K. Morikawa, K. Kobayashi, T. Mizokawa, A. Fujimori, K. Mamiya, F. Iga, H. Kawanaka, Y. Nishihara, A. Delin, and O. Eriksson, Phys. Rev. B **62**, 14304 (2000).

[6] C. Giorgetti, S. Pizzini, E. Dartyge, A. Fontaine, F. Baudelet, C. Brouder, Ph. Bauer, G. Krill, S. Miraglia, D. Fruchart, and J.-P. Kappler, Phys. Rev. B **48**, 12732 (1993).

[7] L. Paolasini, P. Dervenagas, P. Vulliet, J.-P. Sanchez, G. H. Lander, A. Hiess, A. Panchula, and P. Canfield, Phys. Rev. B **58**, 12117 (1998).

[8] L. Paolasini, B. Ouladdiaf, N. Bernhoeft, J.-P. Sanchez, P. Vulliet, G. H. Lander, and P. Canfield, Phys. Rev. Lett. **90**, 057201 (2003).

[9] K. P. Belov, G. I. Kataev, R. Z. Levitin, S. A. Nikitin, and V. I. Sokolov, Sov. Phys. Usp. **26**, 518 (1983).

[10] S. J. Kennedy and B. R. Coles, J. Phys.: Condens. Matter **2**, 1213 (1990).

[11] U. Atzmony and M. P. Dariel, Phys. Rev. B **10**, 2060 (1974).

[12] J.-P. Sanchez, P. Vulliet, and M. M. Abd-Elmeguid, Hyperfine Interact. **133**, 5 (2001).

[13] L. Paolasini and G. H. Lander, J. Alloys Compd. **303-304**, 232 (2000).

[14] Y. Joly, Phys. Rev. B **63**, 125120 (2001). The program can be freely downloaded at www-cristallo.grenoble.cnrs.fr/fdmnes

[15] Y. Joly, S. Di Matteo, and C. R. Natoli, Phys. Rev. B **69**, 224401 (2004).

[16] L. Paolasini, C. Detlefs, C. Mazzoli, S. Wilkins, P. P. Deen, A. Bombardi, N. Kernavanois, F. de Bergevin, F. Yakhou, J.-P. Valade, I. Breslavetz, A. Fondacaro, G. Pepellin, and P. Bernard, J. Synchrotron Radiat. **14**, 301 (2007).

[17] P. C. Canfield and Z. Fisk, Philos. Mag. B **65**, 1117 (1992).

[18] S. J. Kennedy, A. P. Murani, B. R. Coles, and O. Moze, J. Phys. F: Met. Phys. **18**, 2499 (1988).

[19] A. K. Rastogi and A. P. Murani, *Proceedings of the International Conference on Valence Fluctuations, Bangalore* (Plenum, New York, 1986), p. 437.

[20] G. E. Fernandez, M. G. Berisso, O. Trovatelli, and J. G. Sereni, J. Alloys Compd. **261**, 26 (1997).

[21] C. H. Lee, H. Oyanagi, C. Sekine, I. Shirotani, and M. Ishii, Phys. Rev. B **60**, 13253 (1999).

[22] M. K. Sanyal, D. Gibbs, J. Bohr, and M. Wulff, Phys. Rev. B **49**, 1079 (1994).

[23] F. Vaillant, Acta Crystallogr., Sect. A: Cryst. Phys., Diffr., Theor. Gen. Crystallogr. **A33**, 967 (1977).

[24] M. Blume, in *Resonant Anomalous X-Ray Scattering*, edited by G. Materlik, J. Sparks, and K. Fisher (Elsevier, Amsterdam, 1994), p. 495.

[25] *International Tables for Crystallography*, 5th ed., edited by Theo Hahn (Kluwer, Dordrecht, 2002), No. 129.

[26] C. Meneghini, S. Di Matteo, C. Monesi, T. Neisius, L. Paolasini, S. Mobilio, C. R. Natoli, P. A. Metcalf, and J. M. Honig, Phys.

Rev. B **72**, 033111 (2005).

[27] C. Mazzoli, S. B. Wilkins, S. Di Matteo, B. Detlefs, C. Detlefs, V. Scagnoli, L. Paolasini, and P. Ghigna, Phys. Rev. B **76**, 195118 (2007).

[28] H. Fukuda, H. Fujii, H. Kamura, Y. Hasegawa, T. Ekino, N. Kikugawa, T. Suzuki, and T. Fujita, Phys. Rev. B **63**, 054405 (2001).

[29] S. B. Roy, G. K. Perkins, M. K. Chattopadhyay, A. K. Nigam, K. J. S. Sokhey, P. Chaddah, A. D. Caplin, and L. F. Cohen, Phys. Rev. Lett. **92**, 147203 (2004).

[30] P. Carra and B. T. Thole, Rev. Mod. Phys. **66**, 1509 (1994).

[31] S. Di Matteo, Y. Joly, and C. R. Natoli, Phys. Rev. B **72**, 144406 (2005).